Chemical Engineering Journal 522 (2025) 167192

Contents lists available at ScienceDirect

Chemical Engineering Journal

journal homepage: www.elsevier.com/locate/cej

Ammonia tolerant alkaline oxygen reduction reaction on bimetallic cobalt spinels

Karuppasamy Dharmaraj [a,b,*], Rania Hanna [a], Florian Ruske [c], Danielle Douglas-Henry [d], Iver Lauermann [a], Sateesh Prathapani [a,e], Pablo Reyes-Figueroa [a], Yael Rodriguez-Ayllon [f,g], Yan Lu [f,g], Valeria Nicolosi [d], Rutger Schlatmann [a,h], Michelle P. Browne [b], Prashanth W. Menezes [i,j], Sonya Calnan [a,k]

[a] Institute Competence Centre Photovoltaics Berlin, Helmholtz-Zentrum Berlin für Materialien und Energie GmbH, Schwarzschildstrasse 3, 12489 Berlin, Germany
[b] Helmholtz Young Investigator Group Electrocatalysis: Synthesis to Devices, Helmholtz-Zentrum Berlin für Materialien und Energie GmbH, Schwarzschildstrasse 8, 12489 Berlin, Germany
[c] Department Novel Materials and Interfaces for Photovoltaic Solar Cells, Helmholtz-Zentrum Berlin für Materialien und Energie GmbH, Kekuléstrasse 5, 12489 Berlin, Germany
[d] School of Chemistry, CRANN and AMBER Research Centres, Trinity College Dublin, College Green, Dublin D02 PN40, Ireland
[e] QALYTISA Technologies Pvt. Ltd., plot no. 1978, Velaga Heights, Pragathi Nagar, 500090 Hyderabad, India
[f] Institute of Electrochemical Energy Storage, Helmholtz-Zentrum Berlin für Materialien und Energie, Hahn-Meitner-Platz 1, 14109 Berlin, Germany
[g] Institute for Technical and Environmental Chemistry, Friedrich-Schiller-Universität Jena and Helmholtz Institute for Polymers in Energy Applications (HIPOLE Jena), Philosophenweg 7b, 07743 Jena, Germany
[h] Hochschule für Technik und Wirtschaft Berlin HTW, Wilhelminenhofstraße 75A, 12459 Berlin, Germany
[i] Department of Chemistry, Metalorganics, and Inorganic Materials, Technische Universität Berlin, Straße des 17 Juni 135, Sekr. C2, 10623 Berlin, Germany
[j] Department of Materials Chemistry for Catalysis, Helmholtz-Zentrum Berlin für Materialien und Energie GmbH, Albert-Einstein-Strasse 15, 12489 Berlin, Germany
[k] Wolfson School of Mechanical, Electrical and Manufacturing Engineering, Loughborough University, Loughborough, Leicestershire LE11 3TU, England, United Kingdom of Great Britain and Northern Ireland

ARTICLE INFO

Keywords:
Oxygen reduction reaction
Ammonia tolerant ORR catalysts
Half-cell gas diffusion electrodes
Spinels
Direct ammonia fuel cell
In-situ Raman

ABSTRACT

Ammonia, supported by its well-established transportation and distribution infrastructure, is considered as a promising carbon-free hydrogen carrier and emerging as an energy source via low-temperature anion exchange membrane direct ammonia fuel cells (AEM-DAFC). However, ammonia crossover from the anode can poison cathode catalysts, reducing oxygen reduction reaction (ORR) efficiency and cell voltage. Herein, to substitute the state-of-the-art catalyst, Pt/C, and to develop stable, ammonia-tolerant ORR catalysts, monometallic oxides of Co, Fe, Ni, Mn, and bimetallic M-CoO_x (M = Fe, Ni, Mn) were synthesized on gas diffusion electrode (GDE) with microporous layer and tested for ORR activity. Among these, $MnCoO_x$-1 (Mn:Co 1:2) demonstrated high NH_3 tolerance and ORR activity comparable to benchmark fuel cell catalyst, Pt/C under GDE conditions. In-situ Raman spectroscopy performed under GDE conditions revealed that the structure of $MnCoO_x$-1 remains stable, with no detectable changes, even at current densities as high as −25 mA cm^{-2}. During the accelerated stress test conducted at 80 °C with 3.0 M NH_3 in 3.0 M KOH and compressed air at 1.0 bar back pressure feed, $MnCoO_x$-1 showed an overpotential increase of less than 50 mV at −500 mA cm^{-2} in a 1.0 cm^2 membrane electrode assembly type GDE half-cell. Post-mortem X-ray analysis revealed a slight change in the relative atomic composition of $MnCoO_x$-1 after the AST. This comprehensive study reveals that $MnCoO_x$-1 is a stable NH_3 tolerant ORR catalyst, making it a promising cathode candidate for low temperature AEM-DAFC applications.

* Corresponding author at: Institute Competence Centre Photovoltaics Berlin, Helmholtz-Zentrum Berlin für Materialien und Energie GmbH, Schwarzschildstrasse 3, 12489 Berlin, Germany.
E-mail address: karuppasamy.dharmaraj@helmholtz-berlin.de (K. Dharmaraj).

https://doi.org/10.1016/j.cej.2025.167192
Received 25 April 2025; Received in revised form 5 August 2025; Accepted 12 August 2025
Available online 13 August 2025

1. Introduction

Proton exchange membrane fuel cell (PEMFC) technology is quite successful and has gained attention due to its direct zero carbon emission, as the sole reaction product is water [1]. PEMFC utilizes hydrogen oxidation at the anode and oxygen reduction at the cathode as separated by a proton exchange membrane. Researchers are actively working on improving the power density and catalyst durability for wider commercialization [2,3]. However, there are technological barriers for hydrogen storage, compression and transportation, that need to be overcome [4]. As a result, the established transportation and storage network of oxidizable molecules such as alcohols, NH_3 and other liquid organic hydrogen carriers could enable their use in anolyte-based direct fuel cells that could be alternatives to PEMFC [5–7]. Among these, NH_3 is an attractive option as a fuel and hydrogen carrier due to its carbon-free composition and high H_2 content of 17.6 wt%, ease of liquefaction (less than 8 bar at 20 °C), and among other advantages. As a fuel, NH_3 can be directly used through an anion exchange membrane direct ammonia fuel cell, AEM-DAFC, or decomposed into hydrogen for energy applications. In an AEM-DAFC, liquid NH_3 is fed together with KOH or NaOH as the anolyte, and O_2 is fed at the cathode [8,9]. Moreover, the use of an alkaline rather than an acidic electrolyte enhances the oxygen reduction reaction (ORR) which is the limiting reaction in all fuel cells using oxygen as an oxidant. The open circuit voltage at standard conditions of AEM-DAFC is 1.17 *V* which lies close to the PEMFC (1.23 V). Typically, for the anode catalysts, Pt or Pt based alloys are used [10]. However recently, NiCu and other bi-, tri-metallic catalysts have been reported as anode catalysts for AEM-DAFC [11–13]. For the cathode, Pt and as well as several non-noble materials have been reported for the alkaline ORR. However, due to NH_3 crossover through the AEM or separator, the cathode catalyst performance drops through the poisoning by adsorption of N* species from the Gerischer-Mauerer mechanism or Oswin-Salmon mechanism which reduces the overall cell voltage and stability [14]. To overcome the poisoning, Pt based alloys can be used as cathode catalysts since they are known for ammonia electrooxidation. Due to the material scarcity and cost effectiveness, developing non-noble catalysts which are tolerant to ammonia is an attractive option [15]. In this context, transition metal oxide catalysts based on Ni, Mn, Co, and its alloys for the alkaline ORR have already been reported [16–20]. Specifically, Co alloys exhibit high alkaline ORR activity, and in some studies, their activity is superior to the standard Pt/C [21,22]. The better performance of Co rises from the catalyst structure and the synergistic interaction between Co and substrate [23]. However, Co alone shows lower oxygen electrocatalytic activity due to enhanced dissolution and particle agglomeration compared to its alloys [24]. Alloying the Co with metal cations improves the ORR catalysis due to the occupancy of different metal cations at octahedral Co oxide spinels. In principle, the e_g site which refers to high energy d-orbitals of the cations in the octahedral sites acts as the prominent active site for the alkaline ORR compared to Co at the tetrahedral site [25]. All these factors combine to make Co a good candidate for oxygen electrocatalysis.

So far, most of the reported alkaline electrocatalytic ORR studies have been performed using a rotating ring disk electrode (RDE) setup. Though the RDE setup provides the essential information on the catalyst kinetic and thermodynamic parameters unless the catalyst layer is carefully prepared, inaccurate estimation of the intrinsic catalyst activity is likely due to factors like the O_2 diffusion limitations occurring at relatively low overpotentials (and currents), poor adhesion of the catalyst to the support, catalyst agglomeration, imprecise estimate of the catalyst layer thickness, among others [26,27]. Thus, the question arises of how the activity of these transition metal oxides as catalysts behaves under high mass transport conditions required to achieve high current densities for commercial application of alkaline ORR. Further, catalyst evaluation and stability studies under gas diffusion electrode (GDE) conditions are aligned closely with the realistic membrane electrode assembly (MEA) fuel cell setup. Taking these factors into account, we investigated the performance of monometallic (Co, Ni, Fe, Mn) and bimetallic (M-CoO_x, M = Mn, Fe, Ni) catalysts in alkaline ORR under high mass transport conditions using a GDE setup, and whether they withstand NH_3 poisoning. Their ORR performance and stability were thoroughly studied to elucidate their behavior, followed by in-situ Raman measurements in a GDE environment on the stable NH_3 tolerant catalyst.

At first, monometallic oxides (Co, Mn, Fe, Ni) were prepared and their electrocatalytic performance for alkaline ORR along with that of commercial Pt/C, was determined using a GDE half-cell setup with and without NH_3. CoO_x showed the best activity, following that, cobalt containing bimetallic catalysts (M-CoO_x with M = Mn, Fe, Ni) were prepared and evaluated for their tolerance to NH_3 during alkaline ORR. These catalysts were analyzed by various techniques to determine their morphological and chemical characteristics. In-situ Raman measurements on the best NH_3 tolerant catalyst, $MnCoO_x$-1, were performed with and without 0.5 M NH_3 in 1.0 M KOH to evaluate the catalyst structural change under applied currents, using a GDE-Raman cell. Finally, accelerated stress tests (AST) were performed on $MnCoO_x$-1 in both batch and flow type GDE half-cells to investigate the ORR stability in the presence of NH_3 in KOH followed by post-mortem structural and chemical composition characterizations. The effects of O_2 backpressure, electrolyte temperature, KOH concentration, NH_3 concentration, and compressed air as reactants on $MnCoO_x$-1 were also studied and discussed to understand the ORR catalytic behavior under a variety of operating conditions.

2. Results and discussion

2.1. Synthesis, characterization, and electrochemical studies of monometallic oxides

For the ORR study on GDEs, oxides of Co, Fe, Mn, and Ni were first prepared on the commercially obtained carbon cloth gas diffusion electrode (CC) containing a microporous layer (cracks) via electrodeposition (Figs. 1, S1, Table S3). For each deposition, the potential was applied until the charge density reached 0.5C cm^{-2}, unless otherwise stated. Thereafter, the electrodeposited metals were annealed in air at 300 °C resulting in oxides which are described here as CoO_x, FeO_x, MnO_x, and NiO_x. The detailed experimental section is provided in the supporting information file.

Powder X-ray diffraction (pXRD) measurements showed that the synthesized catalysts form metal oxides (Fig. S2). The diffraction peaks of CoO_x and FeO_x match well with the Co_3O_4 and Fe_2O_3 compounds respectively [28–30]. The 2θ peak positions of NiO_x appeared at 37°, 42.9°, 62.6°, 74.9°, and 78.9° matching well with NiO face centered cubic structure of the crystal planes (111), (200), (220), (311), and (222) respectively [31,32]. Formation of poorly crystalline Mn_2O_3 was also observed [33]. Furthermore, X-ray photoelectron spectroscopy (XPS) was used to confirm the formation of Mn_2O_3 which will be

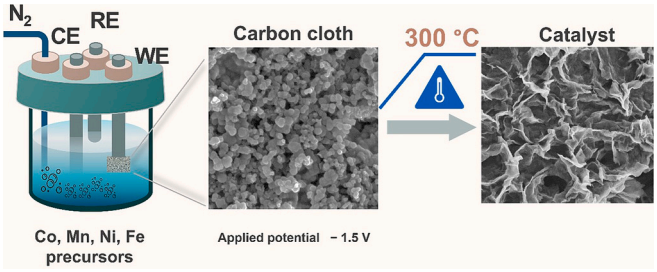

Fig. 1. Schematic of catalyst preparation via electrodeposition starting from precursors followed by annealing in air at 300 °C. RE – Reference Electrode, CE – Counter Electrode and WE – CC Working Electrode.

discussed later. Scanning electron microscopy (SEM) was performed to reveal the surface morphological characteristics of the synthesized catalysts (Figs. S3a-d). NiO_x exhibited nanoparticulate structure while the CoO_x, MnO_x and FeO_x showed fibrous nanosheets. The electrodeposited elements were uniformly distributed on CC as confirmed with energy dispersive X-ray spectroscopy (EDX) (Figs. S3e-l). Further, the chemical states of the synthesized electrocatalysts were analyzed by XPS. The survey spectra of monometallic catalysts are shown in Fig. S4. For the CoO_x, the spin orbit splitting between Co $2p_{3/2}$ and Co $2p_{1/2}$ is 15.4 eV which validates the Co oxide species as Co_3O_4 rather than CoO (15.9 eV) [34]. This shows that the Co oxidized to form Co_3O_4. Peaks at 779.8 eV and 794.8 eV were assigned to Co^{3+} and the peaks at 780.8 eV and 795.8 eV are attributed to Co^{2+} states (Jahn-Teller effect) (Fig. S5a) [34–36]. For the FeO_x, the $2p_{3/2}$ at 711.0 eV matches well with the high-spin Fe^{3+} state agrees with XRD results. The $2p_{3/2}$ peak fits well with multiple components, combined with a satellite at 719.3 eV, showing a difference of 8.3 eV (Fig. S5b) [37–39]. A similar peak split between Fe 3p and the satellite is also observed (Fig. S6). With MnO_x, the core level 2p is split into 641.8 eV and 653.3 eV, corresponding to two spin orbit peaks $2p_{3/2}$ and $2p_{1/2}$ respectively, with a band splitting of 11.5 eV, characteristic of the Mn_2O_3 phase (Fig. S5c) [40]. The peaks located at 641.4 eV, 652.9 eV and 643.1 eV, 654.6 eV can be assigned to Mn^{2+} and Mn^{3+} states respectively [41,42]. Additionally, the Mn 3s peak is split into two components with a binding energy difference of 5.4 eV (Fig. S7) and the O 1s: Mn $2p_{3/2}$ intensity ratio is 1.0 confirming the formation of the Mn_2O_3 compound [43,44]. For the NiO_x catalyst, the peaks in the Ni 2p spectrum at 854.0 eV, 872 eV, and 855.7 eV, 873.3 eV can be assigned to Ni^{2+} and Ni^{3+} valence species respectively (Fig. S5d) [45]. While this assignment is widely used, it remains highly debated due to the multiple splitting of Ni^{2+} and Ni^{3+} photoemission peaks that make deconvolution challenging. However, for simplicity, we adopt the assignment described above while acknowledging the potential quantification challenges it may introduce [46]. This indicates that the catalyst surface contains Ni in the II and III valence states. The O 1s spectra can be fitted to three peaks at 529.8 (±0.3) eV, 531.6 (±0.1) eV and 533.3 (±0.6) eV which were attributed to M-O (M = Co, Fe, Mn, Ni), M-OH (M = Co, Fe, Mn, Ni), and adsorbed water molecules, respectively (Figs. S5e-h). Fig. S8 presents the N_2 adsorption–desorption isotherms and the corresponding pore size distributions of monometallic oxides. The observed Type IV isotherms featuring a hysteresis loop are indicative of mesoporous structures, which are likely attributed to the interlayer spacings inherent to nanosheet morphology. The specific surface areas were determined using the Brunauer-Emmett-Teller (BET) method with a multipoint analysis. Among the monometallic oxides, MnO_x exhibited the highest specific surface area (200 $m^2\ g^{-1}$), consistent with localized pore distribution of 5 nm. In contrast, CoO_x displayed the lowest surface area (49 $m^2\ g^{-1}$) and broad mesopore distribution ranging from 5 to 30 nm, indicating a more compact structure with limited porosity.

For the electrocatalytic studies, the prepared catalysts were tested in the GDE batch type half-cell. The commercially available Pt/C-coated CC (0.2 mg cm^{-2}, 20 % Pt/C, Fuel Cell Store) was also tested as a benchmark (Fig. S9). Polarization curves were obtained through steady state chronopotentiometry (SS-CP) and subsequently corrected for the solution resistance (R_s) measured by galvanostatic electrochemical impedance measurements (GEIS). Fig. S9 shows the polarization curves of CoO_x, FeO_x, MnO_x, and NiO_x catalysts measured in 1.0 M KOH electrolyte at 25 °C with oxygen gas as reactant feed at 200 ml min^{-1}. At low current densities (less than 5 mA cm^{-2}), the prepared catalysts showed identical ORR activity in 1.0 M KOH. The observed ORR overpotentials match with published results on oxides of Ni, Mn, Fe, and Co reported by others [47–49]. Upon increasing the ORR currents, CoO_x, FeO_x, MnO_x, and NiO_x showed an increase in overpotential of about 100 mV, 188 mV, 136 mV, and 200 mV, respectively, compared to Pt/C (0.71 vs RHE) at −100 mA cm^{-2} in 1.0 M KOH. This demonstrates that the tested catalysts behave similarly at low ORR currents and their activity fades at higher current densities. Moreover, for fuel cell applications, catalysts are subjected to high ORR currents, making it essential to test in a GDE half-cell at high current conditions in a laboratory setup. Also, another study using an RDE, showed that the limiting current (<−50 mA cm^{-2}) of CoO_x is much higher than that of NiO_x and MnO_x, which evidences the higher number of electrons transferred at high current densities with less overpotential [18]. Four electron transfer leads to a single step direct reduction of O_2 to OH^- while two electron transfer occurs in 2 steps and requires more energy for complete reduction to OH^-. When 0.5 M NH_3 was added to KOH, the overpotential was further increased to 25 mV, 94 mV, 59 mV, 117 mV, and 57 mV for CoO_x, FeO_x, MnO_x, NiO_x, and Pt/C, respectively, at −100 mA cm^{-2} (Fig. S9). The shift in overpotential in the presence of NH_3 (0.5 M in 1.0 M KOH) for commercial Pt/C was also observed by others [50]. This is due to the catalyst poisoning by the adsorption of N* intermediates, resulting in a reduction of ORR activity [13]. The ammonia exposure to the catalysts also affects the electrochemical surface and area specific activity of the catalyst at applied overpotential [13]. Moreover, the formation of soluble amine complexes with metals like Co, Ni and Fe leads to catalyst dissolution in an alkaline environment that has been extensively reported in metal recovery technology [51]. At low currents, catalyst poisoning is small as the overpotential remains relatively constant. To gain deeper insights, the catalyst kinetics were analyzed using Tafel slopes in 1.0 M KOH (Fig. S10). CoO_x showed a Tafel slope of −111 mV dec^{-1}, suggesting that the first electron transfer step ($M + O_2 \rightarrow MO_2$, where M denotes an active surface site) is the rate determining step [52]. For Co based ORR catalysts, Tafel slope values are similar to those reported by Wu et al. [53]. Other oxides, FeO_x and NiO_x showed Tafel slopes of −79 mV dec^{-1} and −71 mV dec^{-1} respectively, which also coincide with that of Pt/C at −77 mV dec^{-1}. These values suggest a pathway that involves the formation of adsorbed oxygen on the oxide species or the adsorption of oxygen intermediates [52,54]. For the Pt/C, the reported Tafel slopes are in the range of −66 to −75 mV dec^{-1} in KOH electrolyte [50,55]. For the MnO_x catalyst, the Tafel slope is about −116 mV dec^{-1}. In NH_3 containing KOH, the Tafel slopes did not significantly change compared to plain KOH electrolyte, which indicates the ORR mechanism of these monometallic catalysts are not largely affected by the presence of ammonia. A mild shift in Tafel slopes for alkaline ORR in the presence of NH_3 is caused by the change in the O* species adsorption state on the catalyst surface that arises from the increased OH^- concentration on catalyst active sites due to interaction between NH_3 and water [50,56]. Nyquist plots reveal an increase in charge transfer resistance (R_{ct}) and a decrease in electrochemically active surface area (ECSA) for the catalysts in NH_3-containing KOH electrolyte compared to pure KOH (Figs. S11, S12). These findings suggest that N* species likely adsorb onto and block active sites for the ORR. The ORR activity of monometallic oxide catalysts in NH_3-containing KOH follows the order CoO_x > MnO_x > FeO_x > NiO_x, consistent with their intrinsic ORR specific activities normalized to ECSA (Fig. S13). The increase in overpotential at −100 mA cm^{-2} showed that the studied monometallic oxides are less stable at high currents with low catalyst activity towards ORR.

2.2. Synthesis, characterization and electrochemical studies of bimetallic Co oxides

To further improve the ORR activity and to develop stable, ammonia tolerant ORR catalysts, bimetallic oxide catalysts were investigated. Among the monometallic oxides evaluated (CoO_x, MnO_x, FeO_x, NiO_x), CoO_x demonstrated the highest activity at low overpotentials, making Co the optimal choice for bimetallic oxide design. Studies have shown that Co can form spinel phases either as a pure compound or in mixed systems with Fe, Mn, Ni, and Zn [57–60]. In addition, Co based spinel oxides have attracted increasing attention due to their facile synthesis, cost-effectiveness, and robust stability in alkaline ORR. DFT calculations showed that octahedral Co^{3+} species in spinel structure possess optimal binding interaction of the oxygen species with the active center, Co d-

orbitals, thus promoting ORR electrocatalytic activity [61]. Moreover, the Co based spinels have also shown remarkable ORR activity in the presence of organic substances such as methanol, ethanol and ammonia [62–64]. Consequently, we aimed to synthesize bimetallic catalysts ($MnCoO_x$, $FeCoO_x$, $NiCoO_x$) to evaluate ORR performance and also to understand the effect of spinel formation on catalytic activity.

2.2.1. *Effect of Mn on Co oxides*

To start with, bimetallic Co oxides containing Mn using two different Mn:Co molar ratios—1:2 and 2:1—referred to as $MnCoO_x$-1 and $MnCoO_x$-2, respectively were synthesized. The bulk metal ratio of the prepared catalysts was determined with X-ray fluorescence (XRF) analysis (Table S4). The bimetallic $MnCoO_x$ ($MnCoO_x$-1 and $MnCoO_x$-2) showed the nanosheet surface morphology (Fig. S14). pXRD measurements unveiled that both Mn containing oxides $MnCoO_x$-1 and $MnCoO_x$-2 have a $A_{tet}B_{oct}O_4$ spinel structure suggesting the formation of $Co_{2.43}Mn_{0.57}O_4$ [$Co[Co_{1.43}Mn_{0.57}]O_4$] and $Co_{1.74}Mn_{1.26}O_4$ [$Co[Co_{0.74}Mn_{1.26}]O_4$] spinels respectively (Fig. 2a, b, S15, Table S4) [65–67]. These catalysts display Co-rich and Mn-rich phases, respectively [68]. Peaks at 18.5°, 31.2°, 36.7°, 45.6°, 55.1°, 59.2°, 64.8°, and 77.4° are indexed to (111), (220), (311), (400), (422), (511), (440), and (533) respectively. The transmission electron microscopy (TEM) images of $MnCoO_x$-1 reveal a nanostructured material with crystalline domains and planar morphology. The low magnification image shows agglomerated nanoparticles, while the high-resolution TEM confirms the crystallinity through the visible lattice fringes (Fig. 2c, d). Further, the diffraction contrast variation in the Bright-Field-TEM image supports the polycrystalline nature, which is evident from the multiple diffraction spots in the Selected Area Electron Diffraction (SAED) (Fig. 2e). The XPS survey spectra of $MnCoO_x$-1 and $MnCoO_x$-2 are shown in Fig. S16, confirming the presence of Mn and Co elements at the surface. The Co 2p spectra (Figs. 2f, S17a) of the $MnCoO_x$-1 and $MnCoO_x$-2 showed peaks at 779.5–780.5 eV and 794.5–795.5 eV corresponding to Co $2p_{3/2}$ and Co $2p_{1/2}$, respectively, with the energy spacing of 15.4–15.5 eV indicating the presence of Co (III) complexes [69]. The deconvoluted $2p_{3/2}$ peak was fitted with Co^{3+} and Co^{2+} species at 779.9 ± 0.1 eV and 781.4 ± 0.2 eV, respectively, and the peaks at 795.0 ± 0.2 eV and 796.6 ± 0.3 eV were fitted for Co^{3+} and Co^{2+} species of $2p_{1/2}$. The Mn 2p core levels of $MnCoO_x$-1 and $MnCoO_x$-2 consisted of $2p_{3/2}$ and $2p_{1/2}$ peaks at 642.0 eV and 653.5–653.6 eV with a spin orbital splitting of 11.6–11.8 eV which

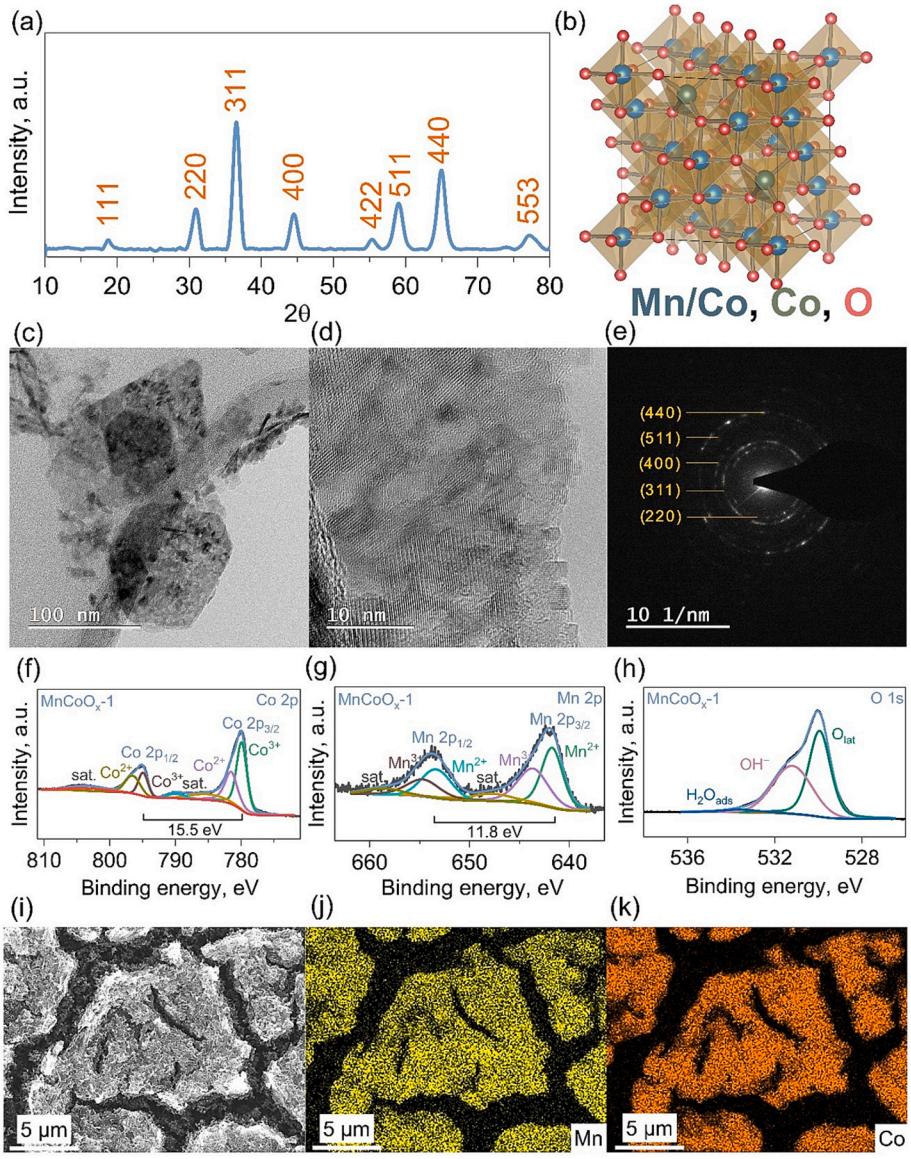

Fig. 2. Characterization of $MnCoO_x$-1: (a) pXRD spectra, (b) $Co[Co\ Mn]O_4$ random spinel lattice model, (c, d) TEM micrographs, (e) SAED pattern, (f-h) XPS core levels of Co 2p, Mn 2p, and O 1s, and (i) EDX elemental mapping highlighting Mn (j) and Co (k) distributions in $MnCoO_x$-1.

corresponds well with previously published findings with dominant Mn^{2+} species (Figs. 2g, S17b) [57,70]. These core levels could be deconvoluted into two Mn species, Mn^{2+} and Mn^{3+} at 641.7–641.8 eV, 653.1–653.5 eV and 643.6–644.0 eV, 654.8–655 eV respectively [71]. This shows that the synthesized catalysts contain the presence of multivalent Co (II, III) and Mn (II, III) species on the surface which is expected for the random spinels. All the satellite peaks are labelled as "sat.". The O 1s spectrum was fitted to three peaks at 529.6 eV, 531.2 eV and 533.4 eV were linked to M-O (M = Co, Mn), M-OH (M = Co, Mn), and adsorbed water molecules species, respectively (Figs. 2h, S17c). EDX analysis revealed that $MnCoO_x$-1 and $MnCoO_x$-2 showed a uniform elemental distribution without any segregation of Mn and Co (Figs. 2i-k, S18). The specific surface areas of $MnCoO_x$-1 and $MnCoO_x$-2 are shown in Fig. S19. $MnCoO_x$-1 exhibits a specific surface area of 128 $m^2\ g^{-1}$ and a pore volume of 0.20 $cm^3\ g^{-1}$, while the $MnCoO_x$-2 sample shows a surface area of 143 $m^2\ g^{-1}$ and a pore volume of 0.49 $cm^3\ g^{-1}$. $MnCoO_x$-1 displays a more localized pore size distribution centred around 5 nm, indicative of a more uniform and compact pore structure, possibly due to denser packing with crystalline domains dominated by CoO. In contrast, the $MnCoO_x$-2 confirms the presence of multiple mesoporous domains likely arising from irregular intersheet spacing within the nanosheet morphology, which spans a range of 5–40 nm.

The $MnCoO_x$-1 and $MnCoO_x$-2 samples were tested for electrochemical ORR activity in 1.0 M KOH in the presence and absence of 0.5 M NH_3 with O_2 as gas feed in a batch GDE half-cell (Fig. 3a, b). Both the tested catalysts, $MnCoO_x$-1, and $MnCoO_x$-2 showed good ORR activity in KOH with an increase in overpotential of 50 mV, and 150 mV, respectively at −100 mA cm^{-2} compared to Pt/C (Fig. 3c). Additionally, the $MnCoO_x$-1 sample showed enhanced ORR activity compared to CoO_x. This is primarily influenced by the presence of Mn in Co spinel for oxygen electrocatalysis [71–73]. A recent study on $MnCoO_x$ suggests that the presence of Mn multi-valence species (Mn^{2+}, Mn^{3+}, Mn^{4+}) specifically Mn^{3+} at octahedral sites, enhances the ORR activity of cobalt spinel [25]. Also, the cation amount to Co ratio greatly influences the ORR activity [75]. This causes the varied ORR performance when the ratio of Mn:Co is changed (Fig. 3c, Table S4). In NH_3 containing KOH, the ORR overpotential at −100 mA cm^{-2} of $MnCoO_x$-1 and $MnCoO_x$-2 increased by 5 mV and 112 mV, respectively, compared to standard KOH electrolyte (Fig. 3c). At low current densities, specifically below −10 mA cm^{-2}, both $MnCoO_x$ samples exhibited identical overpotential for ORR meaning that the catalysts have similar intrinsic activity and the different behavior at higher current density is attributed to a difference in coverage by adsorbed species. Nyquist plots showed lower transfer resistance for $MnCoO_x$-1 than $MnCoO_x$-2 towards ORR in presence of NH_3 (Fig. S20). MnCo oxides showed similar ECSA in 1.0 M KOH. In presence of NH_3, the ECSA of $MnCoO_x$-2 degraded compared to the Co rich $MnCoO_x$-1 catalyst (Fig. S21). Thus, $MnCoO_x$-1 exhibits a more effective ammonia tolerance for alkaline oxygen reduction than $MnCoO_x$-2.

2.2.2. *Effects of Fe and Ni on Co oxides*

To further check the effects of Fe and Ni on Co, $FeCoO_x$ and $NiCoO_x$ catalysts were synthesized with Fe:Co and Ni:Co ratios of 1:2 and 2:1, named as $FeCoO_x$-1, $FeCoO_x$-2, $NiCoO_x$-1, and $NiCoO_x$-2, respectively, using a method similar to that for the $MnCoO_x$ catalyst. These catalysts exhibited morphology and chemical composition comparable to that of the $MnCoO_x$ catalyst, with detailed characterization provided in Table S5 and Figs. S22-S29. The electrochemical activity of $FeCoO_x$-1, $FeCoO_x$-2, $NiCoO_x$-1, and $NiCoO_x$-2 were evaluated in 1.0 M KOH in the presence and absence of 0.5 M NH_3 (Fig. S30). In KOH electrolyte, overpotentials about 160 mV higher compared to Pt/C, were observed for $FeCoO_x$-1 and $FeCoO_x$-2. With NH_3 containing KOH electrolyte, the ORR activity of $FeCoO_x$-1 is diminished, while that of $FeCoO_x$-2 performance remains unchanged. This suggests that $FeCoO_x$-2 is tolerant to NH_3, however, the overall activity is less than that of $MnCoO_x$-1. For the $NiCoO_x$-1 and $NiCoO_x$-2 catalysts, overpotentials at −100 mA cm^{-2} that

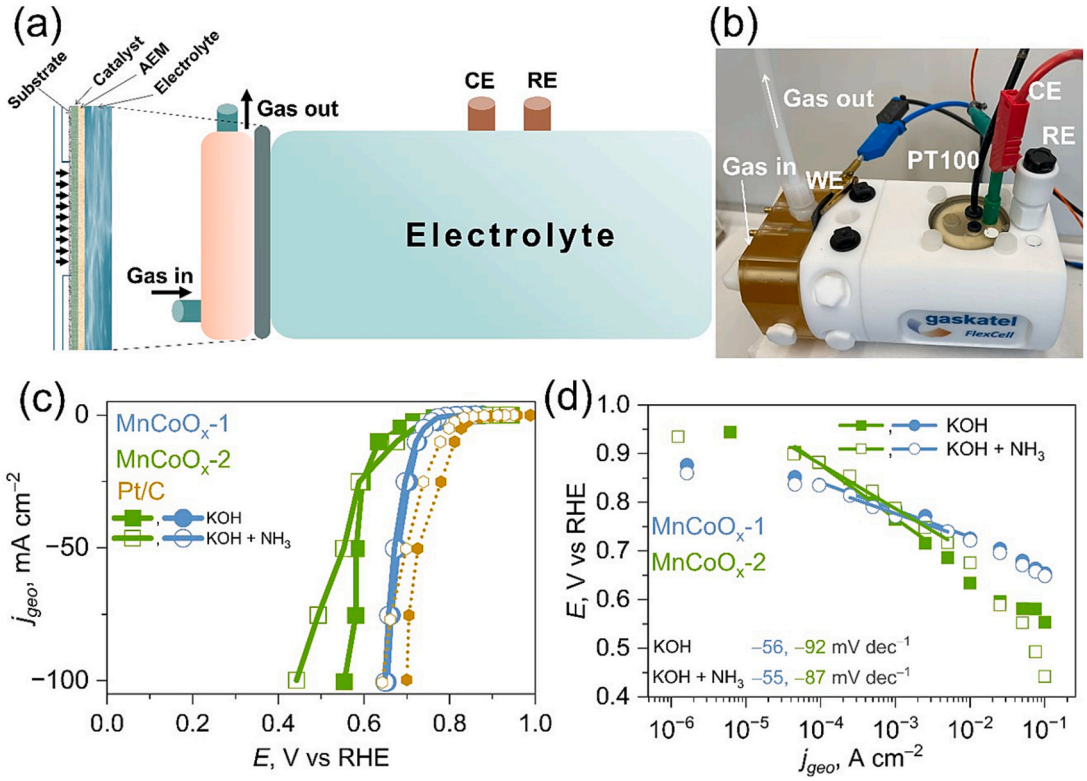

Fig. 3. (a) Schematic representation and (b) photograph of batch type GDE half-cell, (c) SS polarization plot of $MnCoO_x$-1, -2 in KOH with and without NH_3, and (d) SS Tafel plot of $MnCoO_x$-1, -2 in KOH with and without NH_3. The tests were done with an O_2 flow rate of 200 ml min^{-1} at atmospheric pressure and temperature at 25 °C.

were 140 mV and 90 mV higher, respectively, compared to Pt/C were observed. In NH_3 containing KOH, the overpotential increased by a further 65 mV, indicating catalyst poisoning. At low current densities, specifically below −10 mA cm^{-2}, all the synthesized bimetallic oxides exhibited identical overpotential, proving that the catalysts have the same intrinsic activity. However, at −50 mA cm^{-2} and above, catalysts suffer poisoning by N* containing species except for $MnCoO_x$-1. In addition, the overpotential of $MnCoO_x$-1 for ORR above −75 mA cm^{-2} in the presence of ammonia is like that of Pt/C, indicating its potential as an alternative lower cost catalyst for DAFCs (Fig. S31). The overall improved activity of $MnCoO_x$-1 comes from the Mn incorporation into CoO octahedral sites. This was also previously reported where the authors found that Mn addition to the Co facilitates Co^{3+} reduction during the ORR and inhibits the formation of Mn_3O_4 which is less active [18]. The synergistic interaction between the valence states of Mn (II, III) and Co (II, III) improves the ORR activity which is less prominent with Fe and Ni on Co in $FeCoO_x$ and $NiCoO_x$ catalysts [76]. In our kinetics investigation, $MnCoO_x$-1 exhibits a Tafel slope of −56 mV dec^{-1} in KOH (Fig. 3d). In NH_3 containing KOH, it is −55 mV dec^{-1}, showing the faster kinetics towards ORR compared to other bimetallic oxides where the Tafel slopes lie in the range of −80 to −145 mV dec^{-1} (Figs. 3d, S32). This value lies close to the reported Mn—Co catalysts (−43 to −80 mV dec^{-1}) for alkaline ORR [50,55,77]. Notably, the Tafel slope of $MnCoO_x$-1 is close to that of Pt/C (−67 mV dec^{-1}). This is consistent with reports that suggest the adsorbed oxygen coverage mechanism for ORR, that is, high coverage of oxide species or the adsorbed oxygen intermediates [52,54]. On the other hand, $NiCoO_x$-2 and $FeCoO_x$-2 exhibited the Tafel slopes ~−120 mV dec^{-1} which is associated with the first electron transfer step as the rate determining step. Other bimetallic catalysts showed −80 to −100 mV dec^{-1} which is caused by a mixed mechanism [74]. $FeCoO_x$ and $NiCoO_x$ catalysts exhibit comparable charge transfer resistance and electrochemically active surface area, as demonstrated by Nyquist plots and cyclic voltammograms respectively (Figs. S33, S34). Additionally, the intrinsic ORR activity of the catalysts was assessed using ECSA-normalized current densities, revealing that $MnCoO_x$-1 exhibits a lower overpotential than FeCo and NiCo catalysts (Fig. S35).

The Mn content in $MnCoO_x$ catalysts was increased by adjusting the precursor electrochemical bath to a Mn:Co molar ratio of 1:1, and the ORR activity was evaluated. The resulting MnCo (1:1) catalyst exhibited ORR activity comparable to that of $MnCoO_x$-2 in NH_3-containing KOH medium, as shown in Fig. S36. Additionally, the annealing temperature of $MnCoO_x$-1 (MnCo 1:2) was varied to 200 °C and 400 °C to assess its effect on ORR activity (Fig. S37). Samples annealed at 200 °C displayed reduced ORR activity, likely due to the formation of a non-spinel phase. In contrast, samples annealed at 400 °C showed ORR activity comparable to that of $MnCoO_x$-1 annealed at 300 °C in both KOH and NH_3-containing KOH media. These results indicate that optimal Mn:Co ratios and sufficient crystallinity are critical for maximizing ORR activity. The studied mono- and bimetallic catalysts exhibit ORR performance comparable to that reported in recent studies (Table S6). Specifically, the MnCoOx-1 catalyst, synthesized via electrodeposition, demonstrated high oxygen reduction reaction (ORR) activity and NH_3 tolerance in NH_3-containing KOH electrolyte under the tested conditions.

2.3. In-situ Raman study of the active $MnCoO_x$-1 catalyst

Since $MnCoO_x$-1 exhibited the highest ORR activity among the tested bimetallic oxides, we conducted further structural characterization using in-situ Raman spectroscopy. Measurements were performed in 1.0 M KOH and 1.0 M KOH containing 0.5 M NH_3, using an in-situ GDE Raman cell (Fig. S38). Five Raman active peaks are located at about 192, 428, 488, 616, and 688 cm^{-1} corresponding to the characteristic bands ($A_{1g} + E_g + 3F_{2g}$) of Co_3O_4 [78]. Further, peak positions are shifted by a few wavenumbers due to the phonon confinement effect which is consistent with previous reports [79]. As revealed by in-situ Raman studies, the $MnCoO_x$-1 catalyst did not experience substantial changes in the positions of the Raman-active peaks when scanning from low to high current densities, both in the presence and absence of NH_3 in KOH (Fig. 4a, b). This suggests that catalyst structure and random spinel lattice $A_{tet}B_{oct}O_4$ were maintained during the ORR. When the scan direction of the applied current densities was reversed, that is, from −25 mA cm^{-2} to 0 mA cm^{-2}, the Raman spectra were restored back to the initial state, implying that the $MnCoO_x$-1 structure remained stable during the ORR (Fig. S39). Overall, electrochemical and in-situ Raman studies imply that the octahedrally coordinated Mn and Co cations in the spinel structure of $MnCoO_x$-1 exhibit stable and improved ORR activity in both plain KOH and NH_3 containing KOH compared to monometallic and other bimetallic oxides.

2.4. AST on $MnCoO_x$-1 in a batch type GDE half-cell

When the electrodeposition charge density was adjusted to 0.1 and 1.5C cm^{-2}, to vary the loading of $MnCoO_x$-1 the best ORR activity in the presence of NH_3, was observed at 0.5C cm^{-2} (Fig. S40). Examination of the surface morphology shows that lower loadings provide insufficient surface coverage for catalysis, while high loadings impede reactant gas access to the bulk due to excessive coverage (Fig. S41). Additionally, XRF analysis verifies that the Mn: Co ratio remains consistent across different loadings (Table S7). $MnCoO_x$-1 was examined further for stability under AST conditions. The AST condition was adapted and modified from Du, et al. by applying load cycles combined with start-up or shut-down conditions [80]. For the batch cell type measurements, the load cycles were performed by applying the current densities between −25 mA cm^{-2} and −50 mA cm^{-2}, each for 10 s. The detailed protocol is shown in Fig. S42. Fig. S43a shows the polarization curves before and after AST in 1.0 M KOH containing 0.5 M NH_3 at 25 °C. Under low current densities, there is no significant change in overpotential. There is an increase in 35 mV overpotential at −100 mA cm^{-2} after the 9 h of AST. The Nyquist plots from GEIS at current densities of −25 mA cm^{-2} and −50 mA cm^{-2}, showed that the charge transfer resistance remains unchanged after the AST (Fig. S43b). Thus, the AST and EIS results signify that under the tested conditions, the $MnCoO_x$-1 catalyst showed good stability for alkaline ORR in the presence of NH_3. Upon examining the morphology, the catalyst exhibited a polycrystalline nature, but the sample after AST displayed increased crystalline disorder (Fig. S43c, d). The catalyst chemical species were also analyzed before and after AST (Fig. S43e-g). XPS characterization revealed band splitting between Co (Co $2p_{3/2}$ and Co $2p_{1/2}$) and Mn (Mn $2p_{3/2}$ and Mn $2p_{1/2}$) are still maintained at 15.5 eV and 11.8 eV respectively which indicates that the Mn and Co chemical valence species were stable over the 9 h of AST operating condition. The atomic composition between Co and Mn was determined before and after the AST. The relative at. % of Co on the surface showed a reduction of 3 %. It must be noted here that there might be some loss when removing the substrate sandwiched from the membrane. XPS measurements showed the presence of Si impurities that may arise from the substrate (also detected before the AST) and the AEM (Fig. S44). In summary, after 8 h of AST, the minimal increase in overpotential, combined with less structural degradation, proved that $MnCoO_x$-1 was ammonia tolerant under the tested ORR conditions.

2.5. AST on $MnCoO_x$-1 in a MEA type GDE half-cell

To further evaluate the catalyst performance and to mimic the realistic test evaluation in an MEA, the $MnCoO_x$-1 was tested under different backpressure conditions in an in-house developed 1.0 cm^2 flow field type zero gap cell for the three-electrode GDE half-cell measurements (Fig. 5a-c). The GDE half-cell consisted of a reversible hydrogen electrode (RHE) as the reference electrode, carbon felt as the counter electrode, Fumasap FAA-3-50 as the AEM, and catalyst coated CC as the working electrode. The effects of backpressure, KOH electrolyte concentrations, and the effect of ammonia concentrations were initially evaluated in MEA type half-cells (Fig. S45). On increasing from

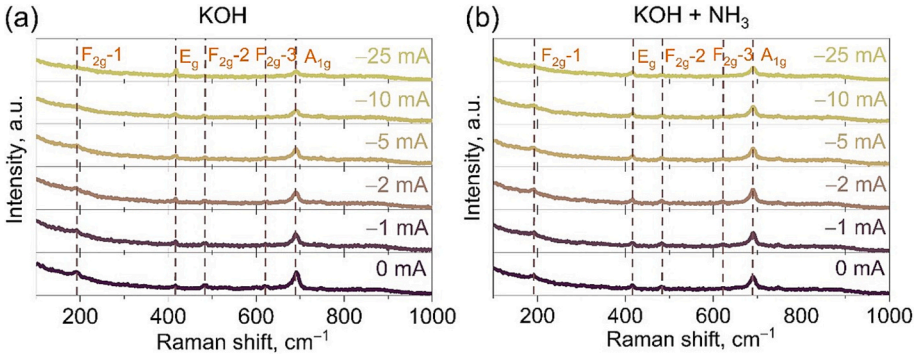

Fig. 4. In-situ Raman spectra of $MnCoO_x$-1 at different applied current densities in (a) KOH and (b) KOH + NH_3 electrolyte.

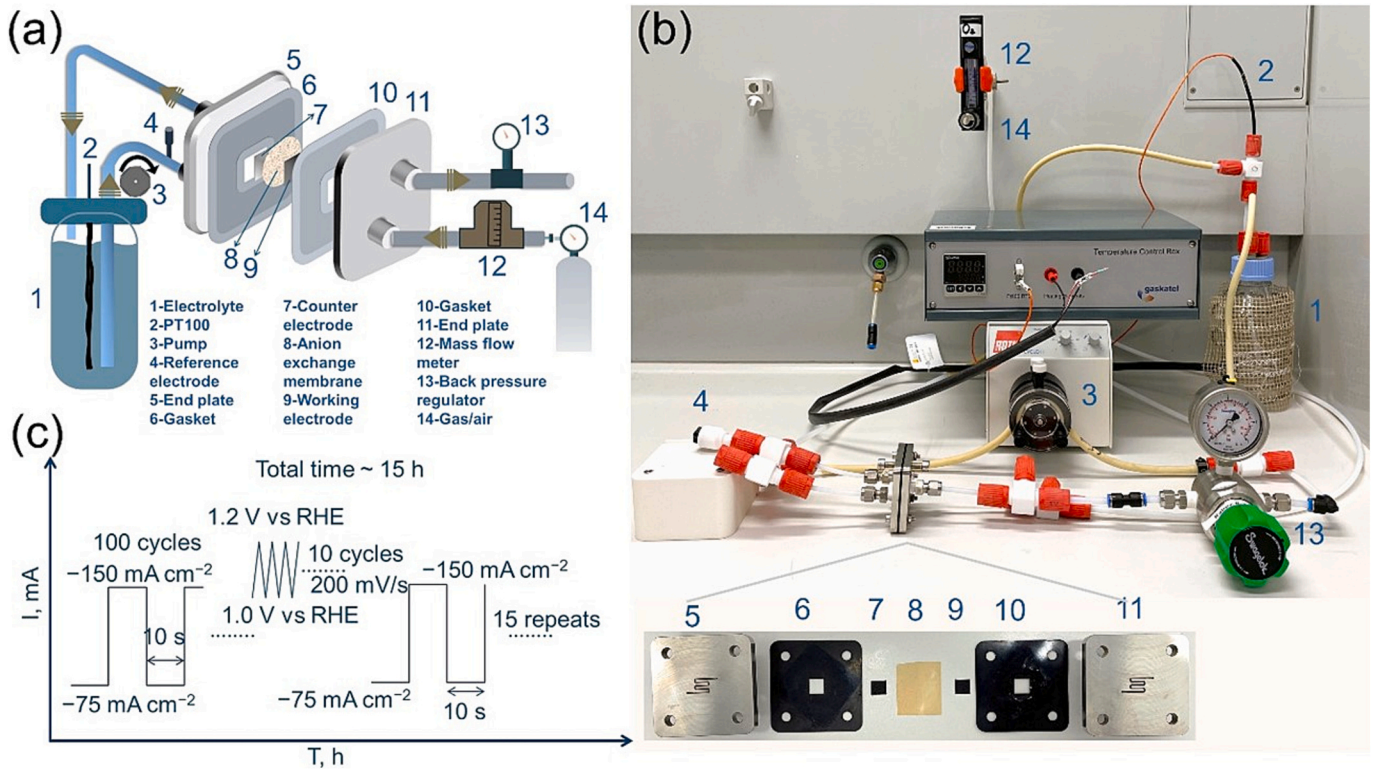

Fig. 5. (a) Schematic representation and (b) digital photograph of zero-gap three electrode flow type GDE half-cell setup, (c) AST protocol of flow cell test.

atmospheric pressure to 0.5 bar backpressure of O_2, there is a reduction in overpotential of 40 m*V* at 1.0 A cm^{-2}. Further increasing to 1.5 bar backpressure, significantly reduced the overpotential to about 75 mV. The reduction in ORR overpotential is likely due to an increase in gaseous reactant on the catalyst surface. Therefore, for further tests, 1.0 bar back pressure was used and the KOH concentrations were varied. The increase in KOH molarity did not substantially reduce the overpotential which further supports that alkaline ORR needs O_2 as a reactant to produce OH^- ions. In addition, the catalyst stability test at a high concentration like 3.0 M KOH is necessary as the anolyte concentration at the anode for DAFC is usually high, enhancing NH_3 crossover, and affecting the overall cell performance. Then, the NH_3 concentration was increased in 3.0 M KOH at 1.0 bar backpressure confirming that a higher ammonia concentration increases the overpotential to about 80 mV at 1.0 A cm^{-2}. This is likely catalyst poisoning due to the presence of a high concentration of adsorbed N* species. The apparent activation energy (E_a) at 0.55 V is found to be 17 kJ mol^{-1} which lies close to the reported value for Pt and Pd catalysts ~20 kJ mol^{-1} in KOH electrolyte (Fig. S46) [81]. The difference in E_a also depends on the measurement setup (RDE vs GDE) used as previously reported by V. Gridin, et al. [82]. The $MnCoO_x$-1 samples were examined further for the stability performance under AST at 1.0 bar backpressure with O_2 and compressed air as gas feed at varying temperatures (40 °C, 80 °C) and NH_3 concentration (1.0 M, 3.0 M) in 3.0 M KOH electrolyte. For load cycles, currents were switched between −75 mA cm^{-2} and −150 mA cm^{-2}, holding each step at 10 s over several hours (Fig. 5c, Table S8). At 80 °C, with compressed air as feed, the potentials were about 400 mV and 200 mV with respect to RHE at −75 mA cm^{-2} and −150 mA cm^{-2} current densities, respectively. SS polarization curves showed that the catalyst overpotential was not considerably increased after the stress test which confirms that the $MnCoO_x$-1 catalyst is relatively stable under these tested conditions where the normal DAFC operates (Fig. 6a, b). The high-resolution TEM image after AST-1 confirms the presence of a crystalline structure (Fig. 6c). $MnCoO_x$-1 was tested using O_2 gas feed under the same conditions and the overpotential at −500 mA cm^{-2} increased by 25 mV after the AST (Fig. S47). In contrast, for different tested conditions, the overpotential at −500 mA cm^{-2} did not significantly increase after the AST. With 1.0 M NH_3 concentration in 3.0 M KOH at 80 °C, both with

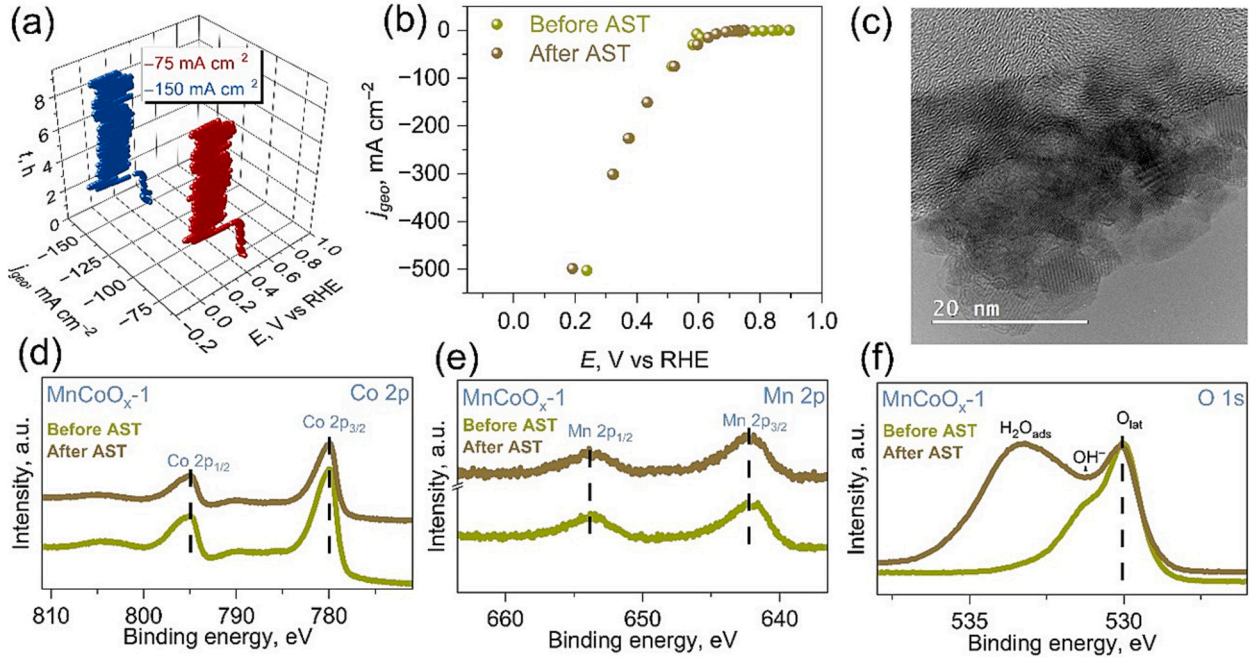

Fig. 6. (a) Time dependent chronopotentiometry during AST, (b) SS polarization curves before and after AST, (c) HR-TEM image after AST, and (d-f) XPS core level spectra of $MnCoO_x$-1 before and after AST in 3.0 M KOH + 3.0 M NH_3. The tests were done with the compressed air flow rate of 200 ml min^{-1} at 1.0 bar back pressure and temperature at 80 °C.

compressed air and O_2 as gas feed, the overpotential increased to 20 mV and 10 mV, respectively, after AST. This explains that nitrogen species poisoning is minimal due to the lower NH_3 content in the electrolyte compared to 3.0 M NH_3 electrolyte tests. At a lower tested temperature, 40 °C, the overpotential increases by 40 mV and less than 5 mV for compressed air and O_2 feed, respectively. This observation agrees with the fact, that catalyst poisoning on the catalyst surface reduces with increasing temperature [83]. The overpotential is quite high for the compressed air as reactant feed compared to pure 100 % O_2 feed at any tests, which is likely due to the lower partial pressure of O_2 in air than pure O_2 gas as feed. Also, the presence of other gases such as N_2, could significantly reduce the O_2 molecules reaching the catalyst electrode surface. This proves that for the long stable operation of DAFC or NH_3 containing fuel cells, the cell needs to be operated at higher temperatures to minimize the cathode catalyst poisoning through membrane crossover. After the AST, the morphological and chemical speciation of the catalysts were analyzed. The morphology of $MnCoO_x$-1 did not vary as confirmed by the SEM images in Fig. S48. TEM images revealed that $MnCoO_x$-1 morphology turned into folds, and the flake size increased while the overall morphology was preserved with minor distortions (Figs. S49a, 6c). SAED shows polycrystallinity was partially maintained while indicating a degree of amorphorisation after AST-2 (Fig. S49b). The valence states of the chemical species, Co and Mn also showed no change as supported by post-mortem XPS analysis except with the minor change (1–3 %) in relative metallic content on the catalyst surface (Figs. 6(d-f), S50). This shows that there is a minimal leaching of Co atoms during the ORR. The above AST and post-AST analyses further provide evidence that $MnCoO_x$-1 could be a suitable NH_3 tolerant ORR catalyst for AEM-DAFC applications (Table S9). We note here that comprehensive testing of electrocatalysts under GDE conditions resembling practical application, using flow-cell-type GDE with variable backpressure, elevated temperatures, and high NH_3 concentrations for the alkaline ORR, is not standard at the time of writing this article.

3. Conclusions

To sum up, we synthesized mono-metallic oxides of Ni, Fe, Co, and Mn and bimetallic oxides of M-Co (M = Mn, Fe, Ni) through electrodeposition technique. Monometallic oxides showed low activity and suffered serious NH_3 poisoning for alkaline ORR. The bimetallic catalysts, $FeCoO_x$, $MnCoO_x$, and $NiCoO_x$ showed better ORR activity than monometallic catalysts. Specifically, the catalyst $MnCoO_x$-1 showed excellent NH_3 tolerance for the alkaline ORR and exhibited low Tafel slopes in NH_3 containing KOH electrolyte. In-situ Raman studies demonstrated that $MnCoO_x$-1 does not undergo substantial structural change as the Raman spectra peaks, three F_{2g}, E_{1g}, and A_{1g} were maintained at −25 mA cm^{-2} in GDE conditions. The NH_3 tolerant ORR stability was evaluated in both batch type and the MEA- mimicking GDE flow cells through AST. The increase in overpotential at −500 mA cm^{-2} is about 25 mV after the AST at 80 °C with O_2 as gas feed in 3.0 M KOH containing 3.0 M NH_3. Furthermore, using compressed air as reactant feed, under the tested conditions, the $MnCoO_x$-1 survived with the overpotential only increasing by 46 mV after AST. The microscopic morphology and metallic ratio were maintained after several hours of operation as confirmed with SEM and XPS analyses. Overall, these results conclude that $MnCoO_x$-1 is one of the best NH_3 tolerant catalysts that can potentially be used in AEM-DAFC applications. Moreover, since the activity, overpotential and Tafel slopes of $MnCoO_x$-1 lie very close to the benchmark Pt/C at high currents, it could also be an alternative cathode catalyst to Pt/C for AEM-DAFC applications.

CRediT authorship contribution statement

Karuppasamy Dharmaraj: Writing – review & editing, Writing – original draft, Validation, Methodology, Investigation, Formal analysis, Data curation, Conceptualization. **Rania Hanna:** Writing – review & editing, Investigation. **Florian Ruske:** Writing – review & editing, Resources, Investigation, Formal analysis, Data curation. **Danielle Douglas-Henry:** Writing – review & editing, Investigation, Formal analysis, Data curation. **Iver Lauermann:** Writing – review & editing, Investigation, Formal analysis. **Sateesh Prathapani:** Writing – review & editing, Investigation, Formal analysis. **Pablo Reyes-Figueroa:** Writing – review & editing, Investigation. **Yael Rodriguez-Ayllon:** Writing – review & editing, Investigation, Formal analysis. **Yan Lu:** Writing –

review & editing, Formal analysis. **Valeria Nicolosi:** Writing – review & editing, Resources. **Rutger Schlatmann:** Writing – review & editing, Supervision, Resources, Project administration, Funding acquisition. **Michelle P. Browne:** Writing – review & editing, Supervision, Resources, Funding acquisition. **Prashanth W. Menezes:** Writing – review & editing, Validation, Supervision, Methodology, Funding acquisition. **Sonya Calnan:** Writing – review & editing, Validation, Supervision, Resources, Project administration, Methodology, Funding acquisition.

Declaration of competing interest

The authors declare that they have no known competing financial interests or personal relationships that could have appeared to influence the work reported in this paper.

Acknowledgements

The authors acknowledge the support from the German Federal Ministry of Education and Research (BMBF) in the framework of the project CatLab (03EW0015A). We acknowledge Wei Zhang from HZB for his support during the N_2 adsorption–desorption isotherms collection. K.D and M.P.B. gratefully acknowledge the Helmholtz Association's Initiative and Networking Fund (Helmholtz Young Investigator Group VH-NG-1719) for the funding. They also thank Christian Schary, Iris Dorbandt, and Maximilian Reinhardt for logistical assistance in organizing the electrochemical experiments. K.D. thanks Axel Zuber and Aline Alencar Emerenciano for providing guidance to the Raman measurements. K.D. also thanks Dorothee Menzel for assisting with the XPS measurements. The Energy Materials In-situ Laboratory (EMIL) operated by the Helmholtz-Zentrum für Materialien und Energie GmbH (HZB) is acknowledged for granting access to its chemistry/sample characterization laboratory. The used SEM is part of the electron microscopy CoreLab (CCMS) of HZB. V.N. and D.D.H. wish to thank the Advanced Microscopy Laboratory in CRANN for the provision of their facilities. This publication has emanated from research supported in part by two grants from Research Ireland under Grant Nos. 12/RC/2278_P2 and 20/FFP-A/8950.

Appendix A. Supplementary data

Supplementary data to this article can be found online at https://doi.org/10.1016/j.cej.2025.167192.

Data availability

Data will be made available on request.

References

[1] Y. Wang, D.F.R. Diaz, K.S. Chen, Z. Wang, X.C. Adroher, Materials, technological status, and fundamentals of PEM fuel cells – a review, Mater. Today 32 (2020) 178–203, https://doi.org/10.1016/j.mattod.2019.06.005.
[2] F. Barbir, S. Yazici, Status and development of PEM fuel cell technology, Int. J. Energy Res. 32 (5) (2008) 369–378, https://doi.org/10.1002/er.1371.
[3] G. Kaur, PEM Fuel Cells: Fundamentals, Advanced Technologies, and Practical Application, Elsevier, 2021, https://doi.org/10.1016/C2020-0-00143-X.
[4] M. Yang, R. Hunger, S. Berrettoni, B. Sprecher, B. Wang, A review of hydrogen storage and transport technologies, Clean Energy 7 (1) (2023) 190–216, https://doi.org/10.1093/ce/zkad021.
[5] Y. Yurko, L. Elbaz, Direct quinone fuel cells, J. Am. Chem. Soc. 145 (4) (2023) 2653–2660, https://doi.org/10.1021/jacs.2c12813.
[6] K. Matsuoka, Y. Iriyama, T. Abe, M. Matsuoka, Z. Ogumi, Alkaline direct alcohol fuel cells using an anion exchange membrane, J. Power Sources 150 (2005) 27–31, https://doi.org/10.1016/j.jpowsour.2005.02.020.
[7] L. Zhai, S. Liu, Z. Xiang, Ammonia as a carbon-free hydrogen carrier for fuel cells: a perspective, Ind. Chem. Mater. 1 (3) (2023) 332–342, https://doi.org/10.1039/d3im00036b.
[8] R. Lan, S. Tao, Direct ammonia alkaline anion-exchange membrane fuel cells, Electrochem. Solid-State Lett. 13 (8) (2010) B83, https://doi.org/10.1149/1.3428469.
[9] G. Jeerh, M. Zhang, S. Tao, Recent progress in ammonia fuel cells and their potential applications, J. Mater. Chem. A 9 (2021) 727–752, https://doi.org/10.1016/10.1039/D0TA08810B.
[10] T. Wang, Y. Zhao, B.P. Setzler, R. Abbasi, S. Gottesfeld, Y. Yan, A high-performance 75 W direct ammonia fuel cell stack, Cell Rep. Phys. Sci. 3 (4) (2022) 100829, https://doi.org/10.1016/j.xcrp.2022.100829.
[11] Z. Liu, M. Wu, J. Ma, Ni–Cu–Co grid-like hydroxyl oxide ammonia oxidation reaction catalyst supported on carbon nanotubes, Energy Fuel 36 (17) (2022) 10339–10345, https://doi.org/10.1021/acs.energyfuels.2c02180.
[12] K. Nagita, Y. Yuhara, K. Fujii, Y. Katayama, M. Nakayama, Ni- and Cu-co-intercalated layered manganese oxide for highly efficient electro-oxidation of ammonia selective to nitrogen, ACS Appl. Mater. Interfaces 13 (24) (2021) 28098–28107, https://doi.org/10.1021/acsami.1c04422.
[13] H. Zhang, W. Chen, H. Wang, X. Tong, Y. Wang, X. Yang, Z. Wu, Z. Liu, A core-shell NiCu@NiCuOOH 3D electrode induced by surface electrochemical reconstruction for the ammonia oxidation reaction, Int. J. Hydrog. Energy 47 (36) (2022) 16080–16091, https://doi.org/10.1016/j.ijhydene.2022.03.139.
[14] R. Abbasi, H. Wang, J.R.C. Lattimer, H. Xu, G. Wu, Y. Yan, Effect of ammonia on the electrocatalysis of oxygen reduction reaction in base, J. Electrochem. Soc. 167 (16) (2020) 164510, https://doi.org/10.1149/1945-7111/abcde1.
[15] R. Chen, S. Zheng, Y. Yao, Z. Lin, W. Ouyang, L. Zhuo, Z. Wang, Performance of direct ammonia fuel cell with PtIr/C, PtRu/C, and Pt/C as anode electrocatalysts under mild conditions, Int. J. Hydrog. Energy 46 (54) (2021) 27749–27757, https://doi.org/10.1016/j.ijhydene.2021.06.001.
[16] Y. Abe, I. Satoh, T. Saito, D. Kan, Y. Shimakawa, Oxygen reduction reaction catalytic activities of pure Ni-based perovskite-related structure oxides, Chem. Mater. 32 (19) (2020) 8694–8699, https://doi.org/10.1021/acs.chemmater.0c03320.
[17] Z. Liang, H. Zheng, R. Cao, Recent advances in Co-based electrocatalysts for the oxygen reduction reaction, Sustain. Energy Fuels 4 (8) (2020) 3848–3870, https://doi.org/10.1039/d0se00271b.
[18] A.C. Queiroz, F.H.B. Lima, Electrocatalytic activity and stability of Co and Mn-based oxides for the oxygen reduction reaction in alkaline electrolyte, J. Electroanal. Chem. 707 (2013) 142–150, https://doi.org/10.1016/j.jelechem.2013.08.039.
[19] F.H.B. Lima, M.L. Calegaro, E.A. Ticianelli, Investigations of the catalytic properties of manganese oxides for the oxygen reduction reaction in alkaline media, J. Electroanal. Chem. 590 (2) (2006) 152–160, https://doi.org/10.1016/j.jelechem.2006.02.029.
[20] C. Goswami, K.K. Hazarika, P. Bharali, Transition metal oxide nanocatalysts for oxygen reduction reaction, Mater. Sci. Energy Technol. 1 (2) (2018) 117–128, https://doi.org/10.1016/j.mset.2018.06.005.
[21] M.S. Ahmed, B. Choi, Y.-B. Kim, Development of highly active bifunctional electrocatalyst using Co_3O_4 on carbon nanotubes for oxygen reduction and oxygen evolution, Sci. Rep. 8 (1) (2018), https://doi.org/10.1038/s41598-018-20974-1.
[22] K. Huang, L. Zhang, T. Xu, H. Wei, R. Zhang, X. Zhang, B. Ge, M. Lei, J.-Y. Ma, L.-M. Liu, H. Wu, −60 °C solution synthesis of atomically dispersed cobalt electrocatalyst with superior performance, Nat. Commun. 10 (1) (2019), https://doi.org/10.1038/s41467-019-08484-8.
[23] H. Jin, R. Yu, C. Hu, P. Ji, Q. Ma, B. Liu, D. He, S. Mu, Size-controlled engineering of cobalt metal catalysts through a coordination effect for oxygen electrocatalysis, Appl. Catal., B 317 (2022) 121766, https://doi.org/10.1016/j.apcatb.2022.121766.
[24] Y. Kiros, Electrocatalytic properties of Co, Pt, and Pt-Co on carbon for the reduction of oxygen in alkaline fuel cells, J. Electrochem. Soc. 143 (7) (1996) 2152–2157, https://doi.org/10.1149/1.1836974.
[25] C. Wei, Z. Feng, G.G. Scherer, J. Barber, Y. Shao-Horn, Z.J. Xu, Cations in octahedral sites: a descriptor for oxygen electrocatalysis on transition-metal spinels, Adv. Mater. 29 (23) (2017) 1606800, https://doi.org/10.1002/adma.201606800.
[26] M. Inaba, A.W. Jensen, G.W. Sievers, M. Escudero-Escribano, A. Zana, M. Arenz, Benchmarking high surface area electrocatalysts in a gas diffusion electrode: measurement of oxygen reduction activities under realistic conditions, Energy Environ. Sci. 11 (4) (2018) 988–994, https://doi.org/10.1039/c8ee00019k.
[27] M. Mazzucato, C. Durante, Comparative analysis of rotating electrode and gas diffusion electrode methods for assessing activity and stability of Fe-N-C based catalysts in ORR, Electrochim. Acta 463 (2023) 142801, https://doi.org/10.1016/j.electacta.2023.142801.
[28] X.Q. Zhao, S. Veintemillas-Verdaguer, O. Bomati-Miguel, M.P. Morales, H.B. Xu, Thermal history dependence of the crystal structure of Co fine particles, Phys. Rev. B 71 (2005), https://doi.org/10.1103/PhysRevB.71.024106.
[29] R.K. Nare, S. Ramesh, P.K. Basavi, V. Kakani, C. Bathula, H.M. Yadav, P. B. Dhanapal, R.K.R. Kotanka, V.R. Pasupuleti, Sonication-supported synthesis of cobalt oxide assembled on an N-MWCNT composite for electrochemical supercapacitors via three-electrode configuration, Sci. Rep. 12 (1) (2022), https://doi.org/10.1038/s41598-022-05964-8.
[30] L.S. Zhong, J.S. Hu, H.P. Liang, A.M. Cao, W.G. Song, L.J. Wan, Self-assembled 3D flowerlike iron oxide nanostructures and their application in water treatment, Adv. Mater. 18 (18) (2006) 2426–2431, https://doi.org/10.1002/adma.200600504.
[31] P. Yang, J. Wang, X. Zhao, J. Wang, Z. Hu, Q. Huang, L. Yang, Magnetron-sputtered nickel oxide films as hole transport layer for planar heterojunction perovskite solar cells, Appl. Phys. A Mater. Sci. Process. 125 (7) (2019), https://doi.org/10.1007/s00339-019-2769-4.
[32] Y. Zhiqiang Wei, Hongxia Qiao, Hua Yang, Cairong Zhang, Xiaoyan, Characterization of NiO nanoparticles by anodic arc plasma method, J. Alloys Compd. 479 (1) (2009) 855–858, https://doi.org/10.1016/j.jallcom.2009.01.064.

[33] F. Gong, S. Lu, L. Peng, J. Zhou, J. Kong, D. Jia, F. Li, Hierarchical Mn_2O_3 microspheres in-situ coated with carbon for supercapacitors with highly enhanced performances, Nanomaterials 7 (12) (2017) 409, https://doi.org/10.3390/nano7120409.

[34] T.J. Chuang, C.R. Brundle, D.W. Rice, Interpretation of the X-ray photoemission spectra of cobalt oxides and cobalt oxide surfaces, Surf. Sci. 59 (2) (1976) 413–429, https://doi.org/10.1016/0039-6028(76)90026-1.

[35] M.C. Biesinger, B.P. Payne, A.P. Grosvenor, L.W.M. Lau, A.R. Gerson, R.St. C. Smart, Resolving surface chemical states in XPS analysis of first row transition metals, oxides and hydroxides: Cr, Mn, Fe, Co and Ni, Appl. Surf. Sci. 257 (7) (2011) 2717–2730, https://doi.org/10.1016/j.apsusc.2010.10.051.

[36] P.W. Menezes, A. Indra, D. González-Flores, N.R. Sahraie, I. Zaharieva, M. Schwarze, P. Strasser, H. Dau, M. Driess, High-performance oxygen redox catalysis with multifunctional cobalt oxide nanochains: morphology-dependent activity, ACS Catal. 5 (4) (2015) 2017–2027, https://doi.org/10.1021/cs501724v.

[37] T. Yamashita, P. Hayes, Analysis of XPS spectra of Fe^{2+} and Fe^{3+} ions in oxide materials, Appl. Surf. Sci. 254 (8) (2008) 2441–2449, https://doi.org/10.1016/j.apsusc.2007.09.063.

[38] A.P. Grosvenor, B.A. Kobe, M.C. Biesinger, N.S. Mcintyre, Investigation of multiplet splitting of Fe 2p XPS spectra and bonding in iron compounds, Surf. Interface Anal. 36 (12) (2004) 1564–1574, https://doi.org/10.1002/sia.1984.

[39] P.S. Bagus, C.J. Nelin, C.R. Brundle, B.V. Crist, N. Lahiri, K.M. Rosso, Combined multiplet theory and experiment for the Fe 2p and 3p XPS of FeO and Fe_2O_3, J. Chem. Phys. 154 (2021) 094709, https://doi.org/10.1063/5.0039765.

[40] M.A. Stranick, Mn_2O_3 by XPS, Surf. Sci. Spectra. 6 (1) (1999) 39–46, https://doi.org/10.1116/1.1247889.

[41] A.G. Abd-Elrahim, D. Roy, M.S. Malik, D.-M. Chun, Low-temperature coating of Mn_2O_3–MoS_2 micro-nano-heterostructure anode as an efficient catalyst for water splitting applications, J. Mater. Sci. 59 (17) (2024) 7332–7355, https://doi.org/10.1007/s10853-024-09620-6.

[42] P.W. Menezes, A. Indra, V. Gutkin, M. Driess, Boosting electrochemical water oxidation through replacement of O_h Co sites in cobalt oxide spinel with manganese, Chem. Commun. 53 (57) (2017) 8018–8021, https://doi.org/10.1039/c7cc03749j.

[43] J.S. Foord, R.B. Jackman, G.C. Allen, An X-ray photoelectron spectroscopic investigation of the oxidation of manganese, Philos. Mag. A 49 (5) (1984) 657–663, https://doi.org/10.1080/01418618408233293.

[44] J.C. Carver, G.K. Schweitzer, T.A. Carlson, Use of X-ray photoelectron spectroscopy to study bonding in Cr, Mn, Fe, and Co compounds, J. Chem. Phys. 57 (2) (1972) 973–982, https://doi.org/10.1063/1.1678348.

[45] M.W. Roberts, R.S.C. Smart, The defect structure of nickel oxide surfaces as revealed by photoelectron spectroscopy, J. Chem. Soc. Faraday Trans. 1 80 (11) (1984) 2957, https://doi.org/10.1039/f19848002957.

[46] A. Grosvenor, M. Biesinger, R. Smart, N. McIntyre, New interpretations of XPS spectra of nickel metal and oxides, Surf. Sci. 600 (9) (2006) 1771–1779, https://doi.org/10.1016/j.susc.2006.01.041.

[47] P. Liu, J. Ran, B. Xia, S. Xi, D. Gao, J. Wang, Bifunctional oxygen electrocatalyst of mesoporous Ni/NiO nanosheets for flexible rechargeable Zn–Air batteries, Nano-Micro Lett. 12 (1) (2020), https://doi.org/10.1007/s40820-020-0406-6.

[48] Y. Pei, D.P. Wilkinson, E. Gyenge, Insights into the electrochemical behavior of manganese oxides as catalysts for the oxygen reduction and evolution reactions: monometallic core-shell Mn/Mn_3O_4, Small 19 (19) (2023) 2204585, https://doi.org/10.1002/smll.202204585.

[49] B. Chutia, P. Bharali, Oxygen deficient interfacial effect in CeO_2-modified Fe_2O_3/C for oxygen reduction reaction in alkaline electrolyte, Catal. Commun. 164 (2022) 106432, https://doi.org/10.1016/j.catcom.2022.106432.

[50] Z. Hu, Q. Xiao, D. Xiao, Z. Wang, F. Gui, Y. Lei, J. Ni, D. Yang, C. Zhang, P. Ming, Synthesis of anti-poisoning spinel Mn–Co–C as cathode catalysts for low-temperature anion exchange membrane direct ammonia fuel cells, ACS Appl. Mater. Interfaces 13 (45) (2021) 53945–53954, https://doi.org/10.1021/acsami.1c16251.

[51] K. Park, D. Mohapatra, B.R. Reddy, C. Nam, A study on the oxidative ammonia/ammonium sulphate leaching of a complex (Cu–Ni–Co–Fe) matte, Hydrometallurgy 86 (3) (2007) 164–171, https://doi.org/10.1016/j.hydromet.2006.11.012.

[52] D.B. Sepa, M.V. Vojnovic, A. Damjanovic, Kinetics and mechanism of O_2 reduction at Pt IN alkaline solutions, Electrochim. Acta 25 (11) (1980) 1491–1496, https://doi.org/10.1016/0013-4686(80)87167-2.

[53] G. Wu, G. Cui, D. Li, P.-K. Shen, N. Li, Carbon-supported $Co_{1.67}Te_2$ nanoparticles as electrocatalysts for oxygen reduction reaction in alkaline electrolyte, J. Mater. Chem. 19 (36) (2009) 6581, https://doi.org/10.1039/b903216a.

[54] X. Ge, A. Sumboja, D. Wuu, T. An, B. Li, F.W.T. Goh, T.S.A. Hor, Y. Zong, Z. Liu, Oxygen reduction in alkaline media: from mechanisms to recent advances of catalysts, ACS Catal. 5 (8) (2015) 4643–4667, https://doi.org/10.1021/acscatal.5b00524.

[55] L. Guo, X. Wan, J. Liu, X. Guo, X. Liu, J. Shang, R. Yu, J. Shui, Revealing distance-dependent synergy between $MnCo_2O_4$ and Co–N–C in boosting the oxygen reduction reaction, ACS Appl. Mater. Interfaces 16 (3) (2024) 3388–3395, https://doi.org/10.1021/acsami.3c15627.

[56] T.J. Schmidt, V. Stamenkovic, J. Ross, P. N., N.M. Markovic, Temperature dependent surface electrochemistry on Pt single crystals in alkaline electrolyte, Phys. Chem. Chem. Phys. 5 (2) (2003) 400–406, https://doi.org/10.1039/b208322a.

[57] P.W. Menezes, A. Indra, N.R. Sahraie, A. Bergmann, P. Strasser, M. Driess, Cobalt–manganese-based spinels as multifunctional materials that unify catalytic water oxidation and oxygen reduction reactions, ChemSusChem 8 (1) (2015) 164–171, https://doi.org/10.1002/cssc.201402699.

[58] D. Lim, H. Kong, C. Lim, N. Kim, S.E. Shim, S. Baeck, Spinel-type $NiCo_2O_4$ with abundant oxygen vacancies as a high-performance catalyst for the oxygen reduction reaction, Int. J. Hydrog. Energy 44 (42) (2019) 23775–23783, https://doi.org/10.1016/j.ijhydene.2019.07.091.

[59] W. Yan, Z. Yang, W. Bian, R. Yang, $FeCo_2O_4$/hollow graphene spheres hybrid with enhanced electrocatalytic activities for oxygen reduction and oxygen evolution reaction, Carbon 92 (2015) 74–83, https://doi.org/10.1016/j.carbon.2015.03.021.

[60] S. Chakrabarty, A. Mukherjee, W. Su, S. Basu, Improved bi-functional ORR and OER catalytic activity of reduced graphene oxide supported $ZnCo_2O_4$ microsphere, Int. J. Hydrog. Energy 44 (3) (2019) 1565–1578, https://doi.org/10.1016/j.ijhydene.2018.11.163.

[61] Z. Wang, J. Huang, L. Wang, Y. Liu, W. Liu, S. Zhao, Z.Q. Liu, Cation-tuning induced d-Band center modulation on Co-based spinel oxide for oxygen reduction/evolution reaction, Angew. Chem. 134 (16) (2022), https://doi.org/10.1002/ange.202114696.

[62] S. Wolf, M. Roschger, B. Genorio, D. Garstenauer, J. Radić, V. Hacker, Ce-modified Co–Mn oxide spinel on reduced graphene oxide and carbon black as ethanol tolerant oxygen reduction electrocatalyst in alkaline media, RSC Adv. 12 (55) (2022) 35966–35976, https://doi.org/10.1039/d2ra06806k.

[63] Y. Zhao, T. Wang, B.P. Setzler, R. Abbasi, J. Wang, Y. Yan, A high-performance gas-fed direct ammonia hydroxide exchange membrane fuel cell, ACS Energy Lett. 6 (5) (2021) 1996–2002, https://doi.org/10.1021/acsenergylett.1c00370.

[64] G. Fu, Z. Liu, J. Zhang, J. Wu, L. Xu, D. Sun, J. Zhang, Y. Tang, P. Chen, Spinel $MnCo_2O_4$ nanoparticles cross-linked with two-dimensional porous carbon nanosheets as a high-efficiency oxygen reduction electrocatalyst, Nano Res. 9 (7) (2016) 2110–2122, https://doi.org/10.1007/s12274-016-1101-2.

[65] C. Ding, J. Lei, Z. Cai, M. Gao, Z. Zou, Y. Li, J. Deng, Catalytic oxidation activation of peroxymonosulfate over Fe-Co bimetallic oxides for flurbiprofen degradation, Environ. Sci. Pollut. Res. 30 (18) (2023) 53355–53369, https://doi.org/10.1007/s11356-023-25914-9.

[66] K.-N. Jung, S.M. Hwang, M.-S. Park, K.J. Kim, J.-G. Kim, S.X. Dou, J.H. Kim, J.-W. Lee, One-dimensional manganese-cobalt oxide nanofibres as bi-functional cathode catalysts for rechargeable metal-air batteries, Sci. Rep. 5 (1) (2015) 7665, https://doi.org/10.1038/srep07665.

[67] A. Jeyaraman, B. Karuppaiah, S.M. Chen, Y. Huang, Development of mixed spinel metal oxide (Co-Mn-O) integrated functionalized boron nitride: Nanomolar electrochemical detection of herbicide diuron, Colloids Surf. A Physicochem. Eng. Asp. 666 (2023) 131278, https://doi.org/10.1016/j.colsurfa.2023.131278.

[68] H. Bordeneuve, A. Rousset, C. Tenailleau, S. Guillemet-Fritsch, Cation distribution in manganese cobaltite spinels $Co_{3-x}Mn_xO_4$($0 \leq x \leq 1$) determined by thermal analysis, J. Therm. Anal. Calorim. 101 (1) (2010) 137–142, https://doi.org/10.1007/s10973-009-0557-7.

[69] D.C. Frost, C.A. McDowell, I.S. Woolsey, X-ray photoelectron spectra of cobalt compounds, Mol. Phys. 27 (6) (1974) 1473–1489, https://doi.org/10.1080/00268977400101251.

[70] M. Harada, F. Kotegawa, M. Kuwa, Structural changes of spinel MCo_2O_4 (M = Mn, Fe, Co, Ni, and Zn) electrocatalysts during the oxygen evolution reaction investigated by in situ X-ray absorption spectroscopy, ACS Appl. Energy Mater. 5 (1) (2022) 278–294, https://doi.org/10.1021/acsaem.1c02824.

[71] C. Walter, P.W. Menezes, S. Orthmann, J. Schuch, P. Connor, B. Kaiser, M. Lerch, M. Driess, A molecular approach to manganese nitride acting as a high performance electrocatalyst in the oxygen evolution reaction, Angew. Chem. 130 (3) (2018) 706–710, https://doi.org/10.1002/ange.201710460.

[72] A. Grimaud, C.E. Carlton, M. Risch, W.T. Hong, K.J. May, Y. Shao-Horn, Oxygen evolution activity and stability of $Ba_6Mn_5O_{16}$, $Sr_4Mn_2CoO_9$, and $Sr_6Co_5O_{15}$: the influence of transition metal coordination, J. Phys. Chem. C 117 (49) (2013) 25926–25932, https://doi.org/10.1021/jp408585z.

[73] T. Sönmez, Studies of Oxygen Electrochemistry on Spinel Oxides, University of Southampton, 2017. http://eprints.soton.ac.uk/id/eprint/415516.

[74] J. Béjar, L. Álvarez-Contreras, J. Ledesma-García, N. Arjona, L.G. Arriaga, Electrocatalytic evaluation of Co_3O_4 and $NiCo_2O_4$ rosettes-like hierarchical spinel as bifunctional materials for oxygen evolution (OER) and reduction (ORR) reactions in alkaline media, J. Electroanal. Chem. 847 (2019) 113190, https://doi.org/10.1016/j.jelechem.2019.113190.

[75] E. Rios, J.-L. Gautier, G. Poillerat, P. Chartier, Mixed valency spinel oxides of transition metals and electrocatalysis: case of the $Mn_xCo_{3-x}O_4$ system, Electrochim. Acta 44 (8–9) (1998) 1491–1497, https://doi.org/10.1016/S0013-4686(98)00272-2.

[76] Y. Yang, Y. Wang, Y. Xiong, X. Huang, L. Shen, R. Huang, H. Wang, J.P. Pastore, S.-H. Yu, L. Xiao, *In situ* X-ray absorption spectroscopy of a synergistic Co–Mn oxide catalyst for the oxygen reduction reaction, J. Am. Chem. Soc. 141 (4) (2019) 1463–1466, https://doi.org/10.1021/jacs.8b12243.

[77] Y. Wang, Y. Yang, S. Jia, X. Wang, K. Lyu, Y. Peng, H. Zheng, X. Wei, H. Ren, L. Xiao, J. Wang, D.A. Muller, H.D. Abruña, B.J. Hwang, J. Lu, L. Zhuang, Synergistic Mn-Co catalyst outperforms Pt on high-rate oxygen reduction for alkaline polymer electrolyte fuel cells, Nat. Commun. 10 (1) (2019), https://doi.org/10.1038/s41467-019-09503-4.

[78] J. Pal, P. Chauhan, Study of physical properties of cobalt oxide (Co_3O_4) nanocrystals, Mater. Charact. 61 (5) (2010) 575–579, https://doi.org/10.1016/j.matchar.2010.02.017.

[79] M. Silambarasan, N. Padmanathan, P.S. Ramesh, D. Geetha, Spinel $CuCo_2O_4$ nanoparticles: facile one-step synthesis, optical, and electrochemical properties, Mater. Res. Express 3 (9) (2016) 095021, https://doi.org/10.1088/2053-1591/3/9/095021.

[80] J. Du, J. Quinson, A. Zana, M. Arenz, Elucidating Pt-based nanocomposite catalysts for the oxygen reduction reaction in rotating disk electrode and gas diffusion electrode measurements, ACS Catal. 11 (12) (2021) 7584–7594, https://doi.org/10.1021/acscatal.1c01496.

[81] Y. Wang, D. Sun, M. Wang, Z. Feng, A.S. Hall, Oxygen reduction electrocatalysis on ordered intermetallic Pd–Bi electrodes is enhanced by a low coverage of spectator species, J. Phys. Chem. C 124 (9) (2020) 5220–5224, https://doi.org/10.1021/acs.jpcc.9b11734.

[82] V. Gridin, J. Du, S. Haller, P. Theis, K. Hofmann, G.K.H. Wiberg, U.I. Kramm, M. Arenz, GDE vs RDE: Impact of operation conditions on intrinsic catalytic parameters of FeNC catalyst for the oxygen reduction reaction, Electrochim. Acta 444 (2023) 142012, https://doi.org/10.1016/j.electacta.2023.142012.

[83] J.J. Ostermaier, J.R. Katzer, W.H. Manogue, Platinum catalyst deactivation in low-temperature ammonia oxidation reactions: I. Oxidation of ammonia by molecular oxygen, J. Catal. 41 (2) (1976) 277–292, https://doi.org/10.1016/0021-9517(76)90343-2.